Available online at www.sciencedirect.com
ScienceDirect
Applied Surface Science 254 (2008) 5061–5072
applied surface science
www.elsevier.com/locate/apsusc

Surfactant-assisted synthesis of defective zirconia mesophases and Pd/ZrO_2: Crystalline structure and catalytic properties

J.A. Wang [a], L.F. Chen [a], M.A. Valenzuela [a,*], J. Salmones [a], D.R. Acosta [b], X. Bokhimi [b], O. Novaro [b,1]

[a] *Escuela Superior de Ingeniería Química e Industrias Extractives, Instituto Politécnico Nacional, Col. Zacatenco, 07738 México D. F., Mexico*
[b] *Instituto de Física, Universidad Nacional Autónoma de México, A. P. 20-364, 01000 México D.F., Mexico*

Received 2 July 2007; received in revised form 28 January 2008; accepted 2 February 2008
Available online 12 February 2008

Abstract

Mesoporous zirconia nanophases with structural defects were synthesized by using a surfactant-templated method. Physicochemical properties and crystalline structures of the zirconia nanophases were studied by means of thermogravimetric analysis (TGA), N_2 physosorption isotherm and *in situ* Fourier transform infrared (FT-IR) spectroscopy, transmission electron microscopy (TEM) and X-ray diffraction (XRD) techniques. The resultant materials show typical mesoporous features which vary with calcination temperature. The cationic surfactant in the network of the solids induces structural deformation and defect creation. The zirconia consists of monoclinic and tetragonal nanophases which contains many structural defects, and its crystalline structure shows microstrain. Both, concentration of lattice defects and degree of the crystal microstrain, decrease as the calcination temperature is increased. When CO is adsorbed on the surface of Pd/ZrO_2, linear bonds of $CO–Pd^0$, $CO–Pd^{\delta+}$ and $CO–Zr^{4+}$ are formed, accompanying with CO_2 production. Catalytic evaluation shows that the Pd/ZrO_2 catalyst is very active for CO oxidation and NO reduction. In the case of oxygen absence from reaction mixture, high selectivity to N_2 is achieved without any NO_2 formation. In the oxygen rich condition, CO conversion is enhanced but less than 19% NO_2 is produced. N_2O is formed only in the reducing condition and its selectivity is sensitive to reaction temperature. The possible mechanisms of NO + CO and NO + CO + O_2 reactions over Pd/ZrO_2 catalyst related to reactant dissociation on the Pd metals and to defective structure of the nanozirconia support are discussed.

Keywords: Zirconia nanophase; Rietveld refinement; Structural defect; Surfactant-templated synthesis; NO reduction; Catalyst

1. Introduction

Since the report by Hino and Arata in 1979 on the synthesis and catalytic application of sulfated zirconia for the isomerization of *n*-butane at 25 °C, sulfated zirconia and zirconia solids have received much attention [1]. Particularly, in conjunction with the Hammett acidity function measurement, sulfated zirconia is regarded as superacid catalyst, which has been suggested to replace the traditional liquid–acidic catalysts in industrial processes of isomerization and alkylation due to the latter causing equipment corrosion and environmental pollution [2,3]. Zirconium oxide has been used as catalyst support for many other catalytic reactions, such as hydrogenation of CO_2 to hydrocarbons (Ru/ZrO_2) and methanol synthesis from synthesis gas (Cu/ZrO_2) [4,5]; bimetallic Pt–Pd on zirconia can be good catalysts for hydrotreating purposes [6]; when WO_3 was deposited on ZrO_2, Brönsted acidity can be created which has great interest for hydroisomerization of hydrocarbons [7]. Due to the presence of structural defects, zirconia is also applied as ionic conductor, oxygen sensor and fuel cell material [8–10]. In addition, recent researches show that ZrO_2 can be also used as NO_x sensor and material for NO_x storage [11,12].

Because of the aforementioned applications, a considerable amount of research work has been devoted to zirconia synthesis and characterization; to date, various methods have been developed to prepare nanosized zirconium oxide [13–20]. Among these, the surfactant-templating technique may be an interesting route to obtain zirconia with mesoporous structure. Sachtler and co-workers reported a mesoporous ZrO_2 prepared by using Zr-isopropoxide in the presence of hexadecane amine as template [13]. The surfactant was successfully removed by

* Corresponding author. Tel.: +52 55 57296000 55112.
E-mail address: mavalenz@ipn.mx (M.A. Valenzuela).
[1] Member of El Colegio Nacional de Mexico.

0169-4332/$ – see front matter © 2008 Elsevier B.V. All rights reserved.
doi:10.1016/j.apsusc.2008.02.015

extraction with ethanol at 80 °C. By using zirconium sulfate as zirconium precursor and cetyltrimethylammonium chloride as template, Ciesla et al. obtained a hexagonal phase of zirconia [14,15]. However, this zirconia is thermal unstable. Sayari et al. used $Zr(SO_4)_2$ as Zr precursor and different quaternary ammonium salts or primary amines as template, as a result, a hexagonal or lamellar ZrO_2 phase was obtained [16].

In the synthesis procedure, when a surfactant is used as a synthesis template, it strongly interacts with the metal ions. As the surfactants are removed from the solid by calcination, some lattice defects are usually created in the corresponding locations of the crystalline structure [21], which is particularly interesting for catalysis since these defects may act as active sites for adsorption or reaction [22]. However, less attention has been paid on the structure defects of zirconia nanophase due to the difficulty in characterizing them. To date, details of the surface and bulk defective structure of nanosized zirconia prepared by using surfactant-templated method have not been reported yet. In addition, since the control of the pore diameter distribution in the solid is of importance from both the scientific and industrial point of view, the effect of the surfactant on the surface structure and texture properties of the zirconia needs further clarification.

This work focuses on the studies of the surface and bulk structure of zirconia solid synthesized by using a cationic surfactant-templated method, in order to gain new insights into the effects of the surfactant in the solid network on the textural and surface properties, and to shed new light on the influences of structural defects and reaction conditions on the catalytic properties in the reaction of NO reduction with CO. The surfactant removal from the solid was carefully monitored by using thermogravimetric analysis (TGA) together with *in situ* Fourier transform infrared (FT-IR) spectroscopy technique; the surface morphological features of the nanozirconia and Pd/zirconia were studied by high resolution electron transmission microscopy (TEM); the crystalline structure was carefully refined by using the Rietveld method on the basis of X-ray diffraction (XRD) analyses. The individual phase concentration, mean crystallite size, lattice cell parameters, average crystal microstrain and defect concentration were quantitatively determined by using the Rietveld method. Moreover, CO chemisorptive properties of the reduced Pd/ZrO_2 samples were measured by means of *in situ* FT-IR techniques under various conditions. Finally, catalytic activity and selectivity of NO reduction and CO oxidation over a 3 wt.% Pd/ZrO_2 catalyst was evaluated under oxygen-absent and -present conditions.

2. Experimental

2.1. Preparation of zirconia and PdO/ZrO_2 solids

The zirconia samples were prepared by using zirconyl chloride octahydrate ($ZrOCl_2{\cdot}8H_2O$) as precursor and a cationic surfactant, cetyltrimethylammonium bromide ($CH_3(CH_2)_{15}N(CH_3)_3Br$, referred as CTAB) as molecular template. In a typical synthesis, 52.5 g of $ZrOCl_2{\cdot}8H_2O$ were dissolved into a container with 500 ml deionized water to form a zirconium solution. This solution was, drop by drop, added into a 3500-ml container that contained a solution of 12.4 g CTAB. The molar ratio of CTAB/Zr is about 1.2 and the pH in the mixture was maintained at 11 by adding ammonia (28 wt.%). To disperse the droplets before the local concentrations become excessive, the mixture was vigorously stirred during the addition. After aging for 24 h, the precipitate was filtered and washed several times by using 500 ml deionized water, and then dried at 80 °C for 2 days followed by calcination at different temperatures (200, 400, 600 and 800 °C) for 4 h in flowing air.

The 3 wt.%Pd/ZrO_2 catalyst was prepared by impregnating the zirconia solid with calculated amount of an aqueous solution of $PdCl_2{\cdot}2H_2O$, the impregnation of $PdCl_2{\cdot}2H_2O$ was performed in one time. The PdO-supported material was dried at 120 °C for 10 h and then was calcined at 600 °C for 4 h. This sample was reduced by 99.9% H_2 at 400 °C for 1 h before CO adsorption measurement and TEM observation.

2.2. Fourier transform infrared spectroscopy (FT-IR)

The surface dehydroxylation and removal of the residual surfactants from the dried samples were characterized by using *in situ* FT-IR spectroscopic technique on a Nicolet Magna-IR 550 spectrometer with a resolution of 4 cm^{-1} over the entire spectral range. The sample wafer was placed in the IR cell, which was linked with a vacuum and heating system. The sample could be exposed in various gaseous environments with various pressures at different temperatures not exceeding 500 °C. The *in situ* FT-IR spectra were recorded at 25, 100, 200, 300 and 400 °C, respectively.

2.3. Textural properties

The specific surface area, pore volume and pore size distribution of the samples were measured in a Digisorb 2600 equipment by using N_2 adsorption–desorption isotherms. Before N_2 adsorption, the samples calcined at 80 and 200 °C were respectively treated at 80 and 200 °C for 14 h under a vacuum condition; while, for the samples calcined at 400, 600 and 800 °C, the thermal treatment was carried out at 350 °C for 2 h. The surface area was determined according to the standard Brunaur–Emmett–Teller (BET) method in a relative pressure range 0.04–0.2 and the total volume was evaluated from the amount adsorbed at a relative pressure of about 0.99. The pore diameter distributions were calculated based on the desorption isotherms by the Barrett–Joyner–Halenda (BJH) method.

2.4. TG-in situ FT-IR analysis

TG analyses were carried out in a Dupont Model 950 thermoanalyzer in air from 25 to 800 °C at a heating rate of 20 °C/min in order to determine the weight loss stages during the thermal treatment and to estimate the amount of the CTAB incorporated into the solids. An infrared spectrometer was coupled on-line with the TG system to analyze the exit gases discharged from the TG system. By analysis of the IR spectra,

the surfactant incorporation into or removal from the solid could be monitored.

2.5. Powder X-ray diffraction and Rietveld refinement

The powder X-ray diffraction data were collected at room temperature in a Siemens D-5000 diffractometer with Cu Kα radiation. The intensities were obtained in the 2θ range between 20 and 110° with a step of 0.02° and a measuring time of 2.67 s at each point. The crystalline structures were refined using FULLPROF98 code with the Rietveld method, which provides not only the concentration and average crystallite sizes of each phase in the sample but also the lattice point defects and microstrain in the crystalline structures [23,24].

For the Rietveld refinement, the zirconia structure was fitted with a tetragonal unit cell with space group $P4_2/nmc$ and a monoclinic unit cell with a symmetry described by $P2_1/C$ space group. The atomic positions of each structure were refined and the lower to upper limits of the coordinates are reported in Tables 1–3. The standard deviations, showing the variation of the last significant figures of the corresponding number, are reported in parentheses. When they correspond to refined parameters, their values are not estimates of the possible error in the analysis as a whole, but only of the minimum errors based on their normal distribution.

The Rietveld software FULLPROF98 is especially designed to refine simultaneously both the structural and microstructural parameters through a least-squares method. Taking into account both the particles size and strain broadening effects, the experimental profiles were modeled with a pseudo-Voigt function. To obtain the quantitative phase abundance of the materials, the individual scale factor was refined with consideration of all refined structural parameters of each phase in our multiphase sample. The weight fraction (W_i) for each phase was then determined from the following refinement relation:

$$W_i = \frac{S_i(NMV)_i}{\sum_j S_j(NMV)_j}\% \quad (1)$$

where i is the value of j for a particular phase among the N phases present. S_j the refined scale factor, N the number of the formula units per cell, M the atomic weight of the formula unit and the V the volume of the unit cell.

2.6. Electron microscopy

The morphological properties of the zirconia samples were studied from electron micrographs obtained in a Philips XL 30 SEM Scanning Electron Microscope; the powder samples were deposited directly on a sample holder covered with a conductive adhesive tape. The analytical electron microscopy observations were carried out with an energy dispersive analysis of X-ray (EDAX) system attached to the scanning electron microscope which was operated at 25 kV. Determination of the chemical composition was based on the average analytical data of individual particles.

High resolution electron microscopic images of ZrO_2 and Pd/ZrO_2 were carried out in a JEOL 4000 EX electron microscope equipped with a pole piece with spherical aberration coefficient of $C_s = 1.00$ mm. The ZrO_2 and Pd/ZrO_2 powder samples were grounded softly in an agate mortar and dispersed in isopropyl alcohol in an ultrasonic bath for several minutes. A few drops were then deposited on 200 mesh copper grids covered with a holey carbon film. The electron micrographs were recorded in electron negative films and in a digital PC system attached to the electron microscope.

2.7. Measurement of CO adsorption

CO (99.9%) was introduced into a H-shape adsorption cell that holds a 3 wt.% Pd/zirconia sample wafer (approximately 10 mg) for CO adsorption. Before adsorption, the sample was thermally treated at 400 °C for 30 min to remove the surface impurities, and the CO adsorption proceeded at 200 °C for 15 min, the IR spectrum was recorded. To study the stability of the CO–Pd band under vacuum, the IR cell was evacuated. The IR spectra were recorded before and after the evacuation in order to compare the variation of the surface bands.

2.8. Catalytic properties

The catalytic evaluation of the Pd/ZrO_2 for NO reduction by CO was performed on a microreactor system under different conditions. In the oxygen-absent condition, the reactants

Table 1
Atomic fractional coordinates of tetragonal zirconia (space group $P4_2/nmc$)

Atom	Site	x	y	z
Zr	2a	0.75	0.25	0.75
O	4d	0.25	0.25	u[a]

[a] $0.035\ (1) < u < 0.050\ (3)$.

Table 2
Atomic fractional coordinates of monoclinic zirconia (space group $P2_1/C$)

Atom	Site	x	y	z
Zr	4e	u_x	u_y	u_z
O (1)	4e	v_x	v_y	v_z
O (2)	4e	w_x	w_y	w_z

Table 3
Limits of the fractional coordinates of monoclinic zirconia

Fractional coordinate	Lower limit	Upper limit
u_x	0.271 (1)	0.275 (1)
u_y	0.0395 (6)	0.0396 (3)
u_z	0.204 (1)	0.210 (4)
v_x	0.061 (7)	0.184 (9)
v_y	0.281 (8)	0.352 (6)
v_z	0.345 (2)	0.385 (7)
w_x	0.446 (2)	0.497 (5)
w_y	0.757 (2)	0.765 (2)
w_z	0.449 (6)	0.478 (3)

mixture fed into the microreactor consisted of 1.5 vol.% CO and 0.5 vol.% NO, the balance was helium; In the oxygen-excess condition, the concentrations of CO, NO and O_2 in inlet mixture were 1.5 vol.%, 0.5 vol.% and 10.5 vol.%, respectively, with helium as balance. In the both conditions, the reactant flow was 30 cm^3/min and reaction temperature ranged from 50 to 400 °C. Catalyst loading was 100 mg. The effluent discharged from the reactor after the reaction was analyzed by on-line gas chromatography-FTIR analysis system (HP-5890 Chemical Station and Nicolet-8220 Gas Analyzer). N_2 and CO_2 were analyzed by gas chromatography and CO, N_2O, NO, NO_2 were analyzed by IR. The light-off temperature, $T_{50\text{-}CO}$, or $T_{50\text{-}NO}$ is defined as the temperature at which the conversion of CO and NO reaches 50%, respectively. For comparison, $T_{50\text{-}CO\text{-}r}$ or $T_{50\text{-}NO\text{-}r}$ is noted as the light-off temperature in the reducing condition and, $T_{50\text{-}CO\text{-}O}$ or $T_{50\text{-}NO\text{-}O}$ the light-off temperature in the oxygen-excess condition.

3. Results and discussion

3.1. Thermogravimetric-IR analysis

The as-prepared sample was thermally characterized by TG-DTG technique (Fig. 1). The TG profile shows several stages of weight loss in a temperature range between 25 and 600 °C. The first stage was below 90 °C that leads to a 4.76 wt.% weight loss. It is assigned to desorption of the loosely bonded water and other adsorbed species like CO_2. In the temperature range between 90 and 250 °C, there was a pronounced step resulting in 12.04 wt.% weight loss. The third stage centered at about 318 °C, yielding a 6.43 wt.% weight loss. The weight losses related to the second and third stages are mostly due to thermal decomposition of the hydrous zirconium oxide and removal of the surfactants linking the material. At 455 °C, another small peak was observed in the TG profile that corresponds to 1.33 wt.% weight loss; it may be caused by combustion of the residual coke or carbonaceous deposits resulting from the oxidation of the surfactant species.

Further information on various weight losses shown in the TG profile was obtained by means of *in situ* FTIR technique. Fig. 2 shows a set of FTIR spectra of the exit gaseous products

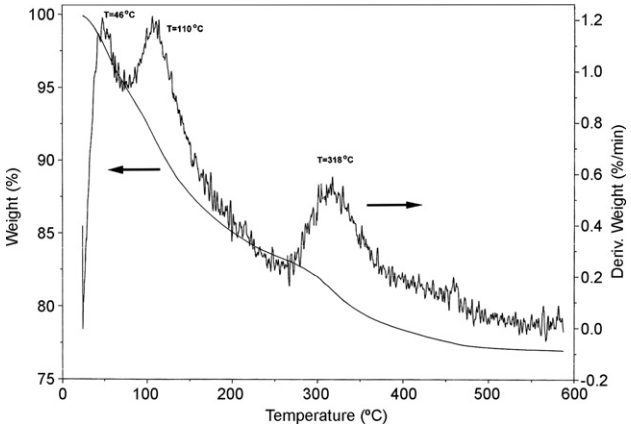

Fig. 1. TG-DTG profile of the dried zirconia solid.

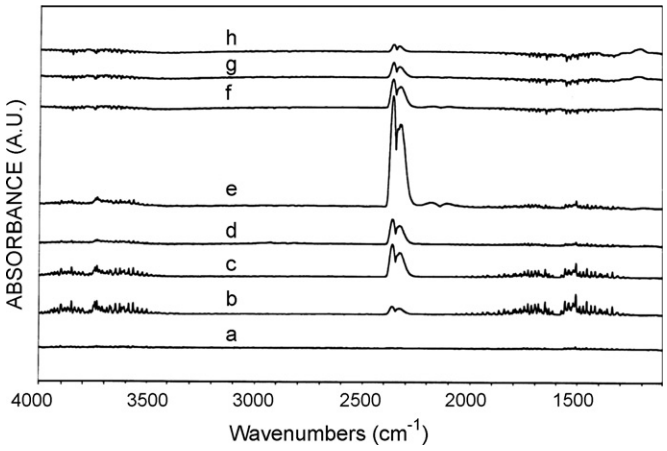

Fig. 2. A set of *in situ* FT-IR spectra corresponding to the exit gaseous mixture discharged from the TGA system: (a) 30 °C; (b) 50 °C; (c) 120 °C; (d) 300 °C; (e) 320 °C; (f) 350 °C; (g) 450 °C; and (h) 550 °C.

discharged from the TG system. In the beginning stage of TG test (30 °C), the IR spectrum exhibited only the base line (Fig. 2a), showing that desorption of water or decomposition of the surfactant did not occur yet. When the TG measurement proceeded to 5 min that corresponds to the peak centered at 50 °C in Fig. 1, the IR spectrum showed several peaks in three groups, i.e., one between 3900 and 3500 cm^{-1} attributed to surface hydroxyls, and another between 1800 and 1300 cm^{-1} (Fig. 2b), these are characteristic of molecular water. This confirms that the first weight loss stage in TG profile is resulted from desorption of adsorbed water. In addition, it is noted that CO_2 was also present in the exit stream since double peaks corresponding to CO_2 appeared between 2400 and 2300 cm^{-1} in the IR spectra. One may find that CO_2 was not detected in the beginning of the TG procedure (Fig. 2a), and at the temperature of 50 °C, the decomposition of the surfactant compounds did not start, hence, the observed CO_2 is likely produced by the desorption of the CO_2 adsorbed on the sample, because the sample was exposed to air before the TG analysis.

In the second weight loss stage of TG (100–250 °C), the materials may undergo crystallization, which can be monitored by analyzing the discharged gaseous products. In this temperature range, the IR peaks corresponding to CO_2 and H_2O were also identified (Fig. 2c). According to the XRD analysis (see the following XRD analysis), below 200 °C, the solid is amorphous, and at 400 °C, the crystalline structure of zirconia appears, indicating that crystallization of the materials takes place in this temperature between 200 and 400 °C. Indeed, in basic conditions the amorphous $Zr(OH)_x$ precipitate is formed, which is unstable and its dehydratation occurs spontaneously, leading to the formation of the zirconium oxohydroxide then to the formation of zirconium oxide ZrO_2. On the other hand, since the intensity of CO_2 bands significantly increased in comparison with the one in the first stage of TG, it is possible that part of the surfactants were oxidized to produce CO_2 in this temperature range. Therefore, the origins of the weight loss in the second stage probably resulted from both the decomposition of hydrous zirconium oxide and oxidation of the surfactant molecules.

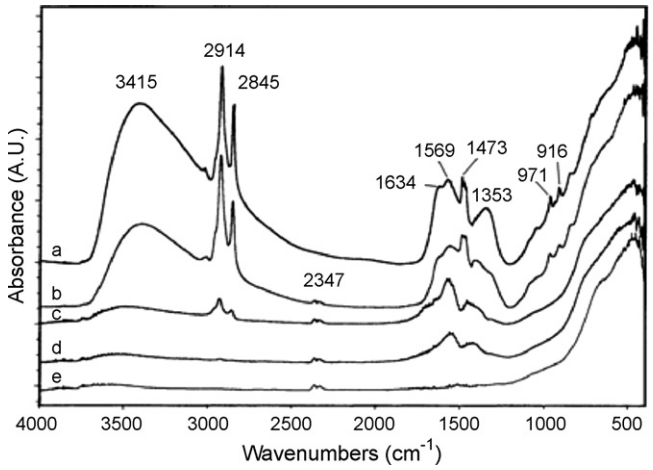

Fig. 3. A set of *in situ* FT-IR spectra of zirconia solid calcined at various temperatures. (a) 25 °C; (b) 100 °C; (c) 200 °C; (d) 300 °C; (e) 400 °C.

In the third weight loss stage (250–430 °C), very sharp peaks corresponding to CO_2 were identified (Fig. 2d, e and f). It is worthy to notice that the intensity of water is very weak in such cases, which significantly differs from that shown in the Fig. 2 b and c. This information strongly indicates that the weight loss between 250 and 430 °C results from the combustion of the residual coke-like deposits produced by surfactant decomposition. Fig. 2g shows the IR spectrum of the gaseous products corresponding to the small peak at 455 °C in Fig. 1. It chiefly consists of CO_2 with almost negligible water, which was probably produced by combustion of residual coke-like deposits. This result indicates that the chemical composition of the related coke-like materials is very hydrogen deficient. The amount of produced CO_2 is clearly diminished at 550 °C (Fig. 2h), confirming that the very small amount of residual carbon-like materials on the sample surface was almost completely removed. The formation and removal of the residual carbon-like materials on the solids was also confirmed by the color changes of the samples during the sample calcination in air. The sample calcined at 80 °C was white; as the calcination temperature increased to 200 and 400 °C, the sample color altered from white to dark gray; after 600 °C calcination, it again changed to white. These observations indicate that the dark gray color was due to the coke-like materials formed on the sample in the temperature range between 200 and 400 °C.

3.2. Surface characterization by in situ FT-IR

Fig. 3 shows a set of *in situ* FT-IR spectra of the as-prepared sample calcined at various temperatures in the IR cell. The material used for IR characterization was dried at 80 °C. When the spectrum was recorded in the IR cell at 25 °C, a wide absorption band appeared in the region between 3700 and 3000 cm^{-1} due to surface OH groups. The twin bands at 2914 and 2845 cm^{-1} are characteristics of the stretching vibrations of C–H bond in hydrocarbons (νCH_{3as} and $\nu(CH_{2as} + \nu CH_{3as})$), i.e. herein the surfactant; in the C–C stretching and C–H deformation vibrations, bands at 1353 and 1473 cm^{-1}, are resulted from the vibration of bending mode of the C–H bonds in the groups of $–CH_2$ and $–CH_3$ in the surfactants [25]. These observations confirm that the surfactant cations are, indeed, linked with the solid during the preparation, they were not removed in washing step. The band at 1634 cm^{-1} is attributed to flextion vibration of the O–H bond. Below 1000 cm^{-1}, the bands are mostly due to Zr–O bond vibration.

When the temperature was raised to 100 °C, the intensities of the bands at 3415 and 1634 cm^{-1} decreased, while, the double bands corresponding to C–H bond at 2914 and 2845 cm^{-1} remained unchanged, indicating that the adsorbed water is partly desorbed, however, the incorporated surfactants have not yet been removed at 100 °C.

As the cell temperature was raised up to 200 °C, it is clearly observed that most of the adsorbed water is desorbed as indicated by a strong diminishing of the broad peak centered at 3415 and the one at 1634 cm^{-1}. The intensities of the bands at around 2800–2920 cm^{-1} and the ones at 1353 and 1473 cm^{-1} were also clearly reduced, showing lower amount of surfactants adsorbed on the surface. It is observed that the band at 1353 cm^{-1} is replaced by a new peak at 1400 cm^{-1}. Considering the possible overlapping of the bands produced by N–O and carbonate-like species, the band at 1400 and 1550 cm^{-1} are probably caused by the N–O or C–OH asymmetrical deformation due to surfactant combustion [26]. In addition, double bands around 2347 cm^{-1} appeared, which are assigned to CO_2. The decrease in the amount of the surfactant and appearance of CO_2 show that decomposition of the incorporated surfactants initially occurs at around 200 °C.

When the temperature was increased to 300 °C, the double bands at 2800–2920 cm^{-1} completely disappeared, revealing that all the surfactants were burnt-off. However, the peaks at 1550 and 1400 cm^{-1} are still visible; at 400 °C, these peaks disappeared too. Only the ones corresponding to CO_2 and very weak band to water are visible at this temperature. This information is in agreement with the results obtained from TG-IR technique shown in Figs. 1 and 2.

3.3. Textural properties

Table 4 shows the data of the BET surface area, mean pore diameter and pore volume of the solids calcined at various

Table 4
Textural data of the zirconium solid calcined at various temperatures

Calcination temperature (°C)	80	200	400	600	800
Surface area (m^2/g)	16.6	76.6	155.3	57.2	26.8
Mean pore diameter (Å)	30.5	31.1	54.0	105.0	144.5
Pore volume (cm^3/g)	0.0385	0.1056	0.2097	0.1944	0.1141

temperatures. The surface area increased from 16.6 to 76.6 and 155.3 m^2/g when the calcination temperature of the solid was elevated from 80 to 200 and 400 °C, and it then declined as the temperature was raised up to 600 and 800 °C. The increment of the surface area below 400 °C must relate to the gradual removal of the surfactant from the solid network. Since the large surfactant ions in the structure occupied some area, after those depart from the solid, new surfaces are created in both the internal or external channels. However, one may find that the pore diameter distribution remains almost unchanged on calcination at 80 and 200 °C (Fig. 4a and b). It shows a very narrow distribution at about 31 Å. Because these two samples retained surfactant in their pores, these surfactants might control the pore diameter distribution. When the sample was calcined at 400 °C, a bimodal pore size distribution was formed and the peak maximum shifts to larger direction compared to the one at 200 °C (Fig. 4c). This may be associated with the heterogeneity of phase composition because the sample

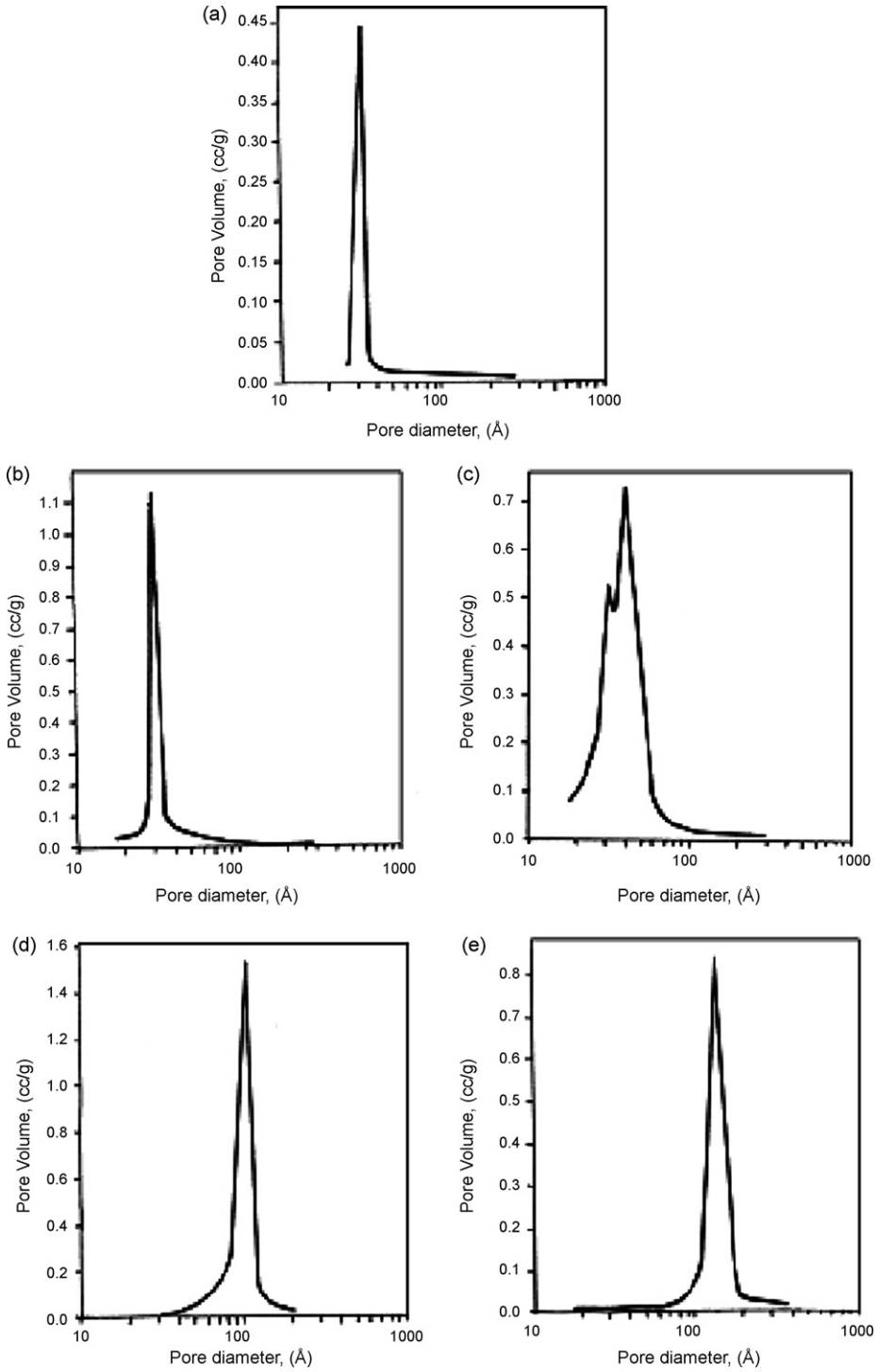

Fig. 4. Pore diameter distribution of the zirconia solid calcined at various temperatures. (a) 80 °C; (b) 200 °C; (c) 400 °C; (d) 600 °C; (e) 800 °C.

underwent phase transformation around 400 °C, the decomposition of hydrous zirconium oxide to zirconia phase was not completely finished yet. This complexity may lead to additional pores forming in the intergranular of different phases present (hydrous ZrO_2 and zirconia), resulting in bimodal distribution of pore size.

When the calcination temperature reached 600 and 800 °C, the average pore diameter increased to 105 and 144 Å (Fig. 4d and e), and the surface area diminished to 57.2 m^2/g and 26.8 m^2/g, respectively. The reduction of the surface area at high calcination temperature is mostly related to partial collapsing of the pore network as well as to the phase transformation from tetragonal to monoclinic phase because monoclinic phase formed at high temperature usually shows lower surface.

3.4. XRD analysis and the Rietveld refinement

Fig. 5 shows the XRD patterns of the zirconia solids calcined at various temperatures. The Rietveld refinement plot of the zirconia calcined at 600 and 800 °C are shown in Figs. 6 and 7. The individual phase concentration, mean crystallite size, lattice cell parameters, average crystal microstrain, atomic occupancy number and cationic defect concentration determined by using the Rietveld method, are reported in the Tables 5 and 6. Below 200 °C of calcination, the solid is an amorphous state. At 400 °C, crystallization occurs, producing fine crystal cores. As the temperature is increased, the crystallite size linearly increases from 5.7 nm at 400 °C to 16.7 nm at 600 °C and to 26.8 nm at 800 °C (Table 5).

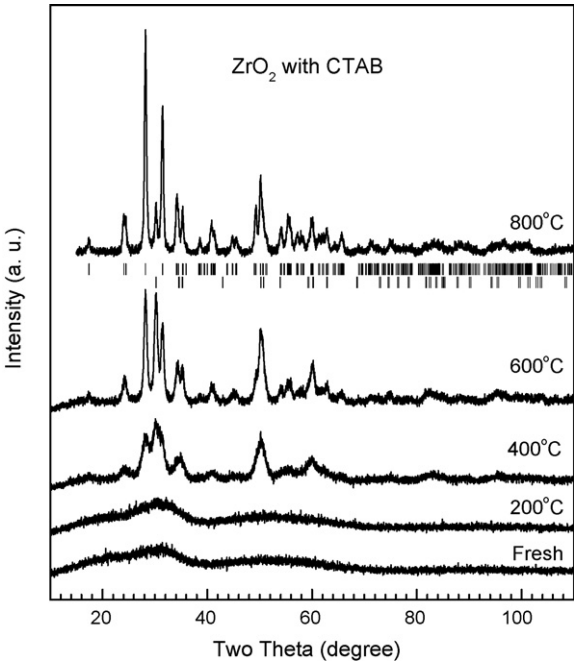

Fig. 5. XRD patterns of the samples (ZrO_2 solid) calcined at 80, 200, 400, 600 and 800 °C. Below the diffraction patterns of the sample calcined at 800 °C, there are two series of tick marks, the upper tick marks correspond to monoclinic zirconia, while the lower ones to the tetragonal phase. These marks are also suitable for indexing the peak positions in the solids calcined at 400 and 600 °C.

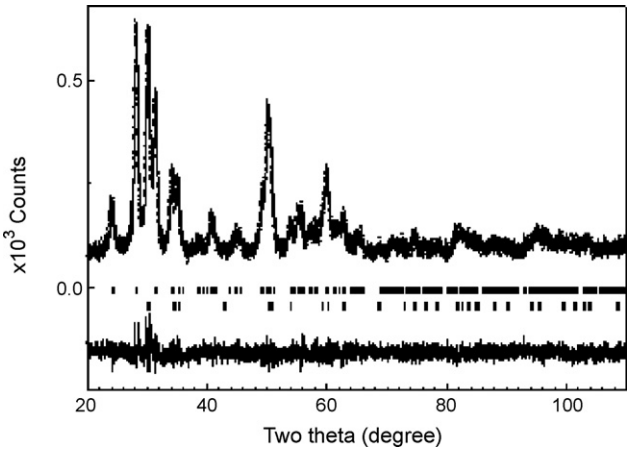

Fig. 6. A Rietveld refinement plot for the zirconia calcined at 600 °C. Experimental data are indicated by square while the calculated curve obtained after the refinement is indicated with a continuous line. Upper tick masks correspond to monoclinic zirconia. The lower one to the tetragonal phase. The continuous curve under the tick marks represents the difference between the experimental and the calculated data.

The zirconia solids calcined at different temperatures consist of both monoclinic (m-ZrO_2) and tetragonal (t-ZrO_2) phases, but the monoclinic phase is the major (Tables 5 and 6). Increasing calcination temperature leads to phase transformation from tetragonal to monoclinic. For example, when the temperature increased from 600 and 800 °C, the concentration of monoclinic phase raised from 69 and 91 wt.%.

The structural refinements confirm that the monoclinic structure contains lattice defects and it suffers strong microstrain. The defect concentration and the degree of microstrain vary with calcination temperature (Tables 5 and 6). The degree of crystalline structure imperfection is largely dependent of the surfactant in the network of the zirconia solid that can be explained by a mechanism responsible for phase transformation during the calcination, which may include continuous bond rupture and formation, local temperature rises, microdeformation of the surface and hydrostatic stresses

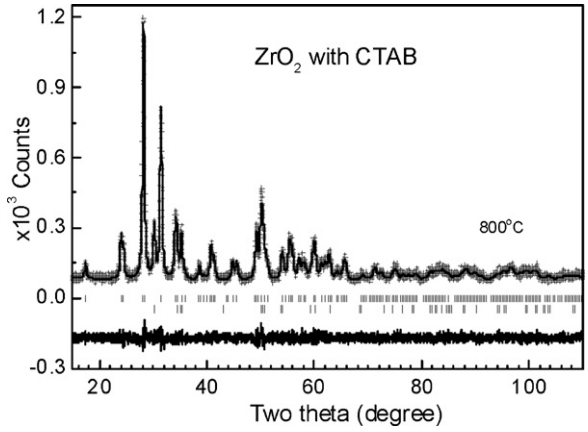

Fig. 7. A TEM micrograph of the ZrO_2 sample calcined at 800 °C. Experimental data are indicated by square while the calculated curve obtained after the refinement is indicated with a continuous line. Upper tick masks correspond to monoclinic zirconia. The lower one to the tetragonal phase. The continuous curve under the tick marks represents the difference between the experimental and the calculated data. $R_{wp} = 0.11$.

Table 5
Data of average crystallite size, phase concentration, lattice parameters, cation occupancy number, and zirconium defect number per unit cell in the zirconia monoclinic phase (m-ZrO_2) at different annealing temperatures

Calcination temperature (°C)	400	600	800
Average crystallite size (nm)	5.7 (2)	16.7 (3)	26.8 (5)
Phase concentration (%)	69 (5)	69 (3)	91 (6)
Cell parameter *a* (nm)	0.5145 (5)	0.5181 (5)	0.51315 (5)
Cell parameter *b* (nm)	0.5146 (1)	0.5202 (2)	0.5316 (1)
Cell parameter *c* (nm)	0.51457 (6)	0.52052 (7)	0.53143 (7)
Average crystal microstrain (%)	1.8 (5)	1.4 (2)	1.2 (1)
Zr atom occupancy number	0.7050 (1)	0.8499 (1)	0.8325 (1)
Zr defect number in unit lattice cell	1.18	0.60	0.63

[27,28]. The strong interactions between the deprotonated hydroxyl groups and the positively charged surfactant headgroups, leads to surfactant cationic strongly interacting with the Zr–O–Zr framework, thus forming a polymeric network of hydrous oxides. These surfactant cations were difficult to be removed by simple wash with water or methanol. However, at a proper calcination temperature, i.e., 300–400 °C, when they burn off, cationic lattice defects may be generated in the corresponding locations of the crystalline structure.

It is worthy to note that phase composition influences the formation of structural defects. The tetragonal zirconia phase usually shows oxygen defects in its structure that makes possible to use it as oxygen sensor material; in the monoclinic zirconia structure, however, as shown in this work, there exists cationic lattice defects. In our sample, the main phase is monoclinic; therefore, cationic lattice defect is one of the structure features of the zirconia prepared through the surfactant-controlled route in a base condition. This result reveals that for obtaining zirconia nanophases with desired structure defect, the phase composition of the zirconia is the primary factor that could be controlled by varying the preparation parameters.

The zirconia crystals contain microstrain which strongly varies with the calcination temperature. The average of the crystallite microstrain decreased from 1.8% at 400 °C to 1.4% 600 °C and to 1.2% at 800 °C. The zirconia structures show strong distortion due to the presence of cationic lattice defects. The average crystalline microstrain reduced with the temperature increasing. This is because that the degree of the structure order increased at higher calcination temperature due to defect concentration deminishing.

3.5. Electron microscopy observation

The goals in high resolution electron microscopy observations were to detect and localize the metallic phase in the ZrO_2 crystallites and to identify the presence of structural details. The metallic palladium phases were observed like a great number of dark and small particles (Fig. 8). Though the metallic particles were anchored into the zirconia support, the transparency and unaltered lattice ZrO_2 planes still could be clearly observed. The Moire fringes observed in the overlapped crystals tell us about the planar and thin layer configuration of the ZrO_2 support grains.

Table 6
Data of average crystallite size, phase concentration, and lattice parameters for the zirconia tetragonal (t-ZrO_2) phase at different annealing temperatures

Calc. temp. (°C)	400	600	800
Average crystallite size (nm)	6.3 (2)	17.2 (7)	21 (1)
Phase concentration (%)	31 (3)	31 (1)	9 (1)
Cell parameter *a* (nm)	0.3592 (2)	0.3596 (1)	0.3598 (1)
Cell parameter *c* (nm)	0.5182 (5)	0.5184 (2)	0.5184 (3)

A considerable degree of structural defects were also directly observed in the HRTEM micrographs. The crystalline structure in some zones of the ZrO_2 crystals are well ordered; while, in other zones, rather disordered arrangements are observed (Fig. 9). Even in the ordered zone, some pore walls disappeared as indicated by white arrows, showing that structural defects are formed (Fig. 10). These observations are also in agreement with the results obtained from the Rietveld refinement.

In combination of the results obtained from TG, FT-IR, BET and XRD analyses, it is possible for us to picture a relatively complete procedure of the zirconia nanophase formation. In the synthesis process, since the precipitation of zirconium cations (Zr^{4+}) was carried out in a basic condition (pH 11), the positively charged zirconium ions are easily hydrated to form complexes with OH^- and water molecules formulated like $Zr(OH)_x^{(4-x)-}\cdot yH_2O$. When the surfactant is present, these complex hydroxides can be further polymerized and precipitated to produce polymeric hydrous oxide containing cetyltrimethylammonium cations; it transforms as inorganic/

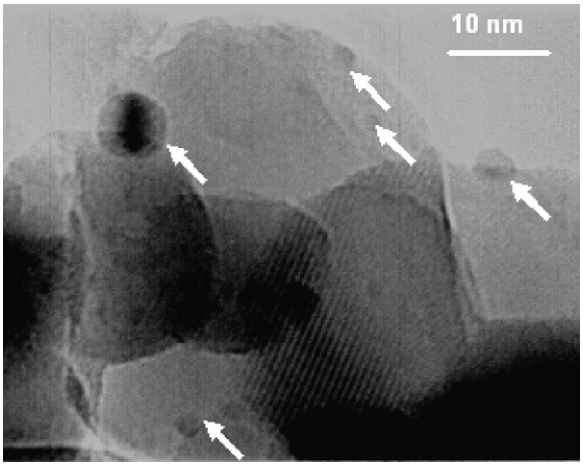

Fig. 8. A HRTEM micrograph of the 3 wt.% Pd/ZrO_2 sample. The anchored metallic particles are clearly observed.

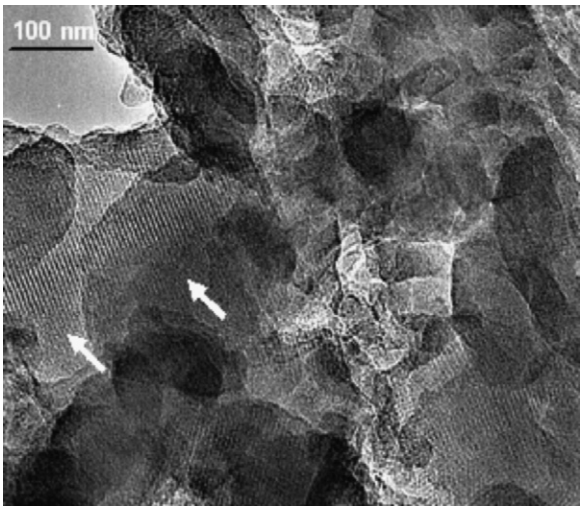

Fig. 9. A HRTEM shows the crystal twins and lattice defects in the ZrO_2 structure. HRTEM micrographs of the zirconia solid calcined at 600° C. There are dislocations and structural defects in many zones as indicated by the white arrows.

organic composites like $Zr(OH)_n(O\text{-surf})_m$; after drying and calcination in air, a mesoporous zirconia nanophase was finally formed as the dehydratation occurred and the surfactant was decomposed and oxidized. These multi-processes can be represented as following steps (i) through (vi):

(i) Formation of zirconium hydroxide in the precipitation

$$Zr^{4+} + yH_2O + xOH^- \rightarrow Zr(OH)_x{}^{(4-x)+}\cdot yH_2O \quad (2)$$

(ii) Surfactant incorporation during the synthesis

$$Zr(OH)_x{}^{(4-x)+}\cdot yH_2O + \text{surfactant} \rightarrow Zr(OH)_n(O\text{-Surf})_m\cdot yH_2O \quad (3)$$

(iii) After drying at 80 °C

$$Zr(OH)_n(O\text{-Surf})_m\cdot yH_2O \rightarrow Zr(OH)_n(O\text{-Surf})_m + yH_2O \quad (4)$$

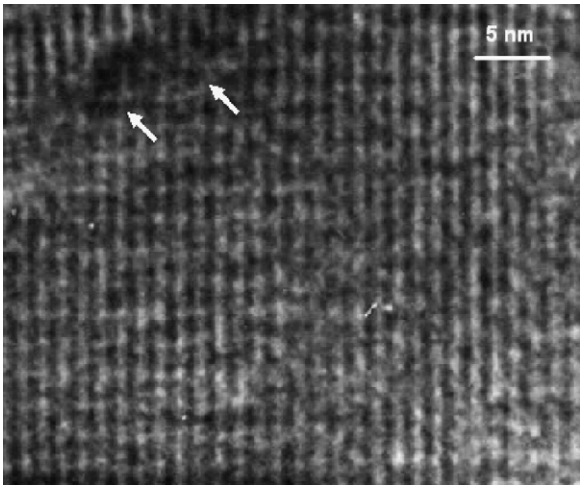

Fig. 10. The HRTEM micrographs of the zirconia solid calcined at 600 °C. It is shown that the crystalline structure contains some lattice defects and dislocations. HRTEM show structure defects in the ZrO_2 crystal calcined at 600° C. The white arrows indicate location of the structural defects.

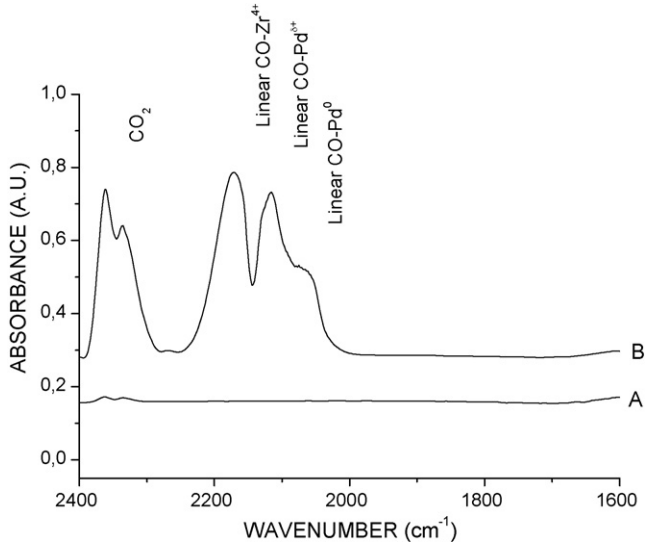

Fig. 11. FT-IR spectra of CO adsorption on the 3 wt.% Pd/ZrO_2 under various conditions. A variety of linear CO-metal bonds were formed after CO adsorption. (A) Before CO adsorption, 400 °C. (B) After CO adsorption at 200 °C, the sample was evacuated to 20 Pa.

(iv) In the temperature range between 100 and 250 °C

$$Zr(OH)_n(O\text{-Surf})_m + O_2 \rightarrow \text{amorphous}ZrO_2 + \text{coke-likedeposit} + CO_2 + H_2O \quad (5)$$

(v) Zirconia crystallization and dehydroxylization

$$\text{amorphous}ZrO_2 \rightarrow \text{t-}ZrO_2 + \text{m-}ZrO_2 \quad (6)$$

(vi) In the temperature from 250 °C up to 800 °C

$$\text{coke-likematerials} + O_2 \rightarrow CO_2 + H_2O \quad (7)$$

$$\text{t-}ZrO_2 \rightarrow \text{m-}ZrO_2 \quad (8)$$

3.6. CO adsorption properties on Pd/ZrO_2

CO adsorption–desorption behavior on the palladium supported zirconia analyzing by *in situ* FT-IR spectroscopy was also studied because of the importance of the Pd/ZrO_2 as catalyst for CO elimination in the automobile emissions. Fig. 11 shows a set of *in situ* FT-IR spectra before and after CO adsorption on a 3%Pd/ZrO_2 calcined at 800 °C. The spectra were recorded at different conditions including various temperatures and atmospheres. Two groups of adsorption bands were observed: one group consists of two peaks appearing in the range 2400–2280 cm^{-1} and another has three peaks between 2250 and 2000 cm^{-1} (Fig. 11B). Generally, two adsorption modes of CO–Pd, linear and bridged bonds, are usually observed in the case of CO adsorption on Pd atom clusters or crystals. The wavenumber of the CO–Pd^0 linear bond and the bridged bond appears in the range of 2100–2000 cm^{-1} and 1900–2000 cm^{-1}, respectively. Based on these well-known assignments, the bridged form of CO adsorption on Pd atoms was not formed on our sample because no band in 1900–2000 cm^{-1} range was observed (Fig. 11B). The absorption band at 2065 cm^{-1} was due to CO adsorbed on the Pd^0

atoms in a linear mode. The one at 2169 cm^{-1} was mostly due to the CO adsorbed on zirconium ions in the support in a linear form (Zr^{4+}–CO) similar to the one observed in the case of CO adsorption on CeO_2 and TiO_2 [29]. It is reported that CO adsorbs on Pd^+ or Pd^{2+} ions in the Pd/CeO_2 sample may form CO–Pd^+ or CO–Pd^{2+} bonds, the former shows peak at the range 2100–2112 cm^{-1} and the latter between 2115 and 2160 cm^{-1} [30,31]. Therefore, the band at about 2113 cm^{-1} in Fig. 11B is assigned to CO linearly adsorbed on $Pd^{\delta+}$ sites ($0 < \delta < 2$). The oxidation of originally reduced Pd atoms in our sample may have occurred by oxygen generating from CO dissociation on Pd metals. The twin bands at 2337 and 2358 cm^{-1} are attributed to the adsorbed CO_2. As shown in the Fig. 11A, before exposure to CO environment, the sample shows very weak bands corresponding to CO_2, indicating that trace amount of CO_2 exists in the IR adsorption cell. After CO adsorption, the twin bands show a salient growth in intensity. Therefore, the increment of CO_2 concentration must be resulted from CO in the course of adsorption. CO_2 may be yielded by CO reacting with surface lattice oxygen in the support Because CO oxidation reaction easily takes place on the Pd-based catalyst surface at approximately 200 °C as evidenced by the catalytic test in an oxygen-absent case as reported in the following section. When CO was allowed to the IR cell at 200 °C, CO reacts with surface oxygen of the solid to produce CO_2.

After the IR cell was evacuated, all the IR peaks disappeared, indicating that the bounded CO and CO_2 were desorbed from the active sites. Strong adsorption of either the reactant or product may poison the active sites and leads to catalyst rapid deactivation. Possible removal of both the adsorbed CO and CO_2 at 200 °C is in favorable to refreshing the active sites when the Pd/ZrO_2 is used as catalyst, i.e., for CO oxidation to CO_2, and for NO reduction *via* CO.

3.7. Catalytic activity and selectivity

3.7.1. In the oxygen absence condition

Catalytic activity and selectivity of NO reduction by CO over the Pd/ZrO_2 catalyst are reported in Table 7. In the case of oxygen absence from the inlet mixture, the light-off temperature for NO reduction was between 100 and 150 °C and for CO oxidation between 150 and 200 °C. The catalytic activity for both CO oxidation and NO reduction enhanced as the reaction temperature was increased. N_2O was formed during the reaction, but the selectivity to N_2O strongly depended upon the reaction temperature. N_2O production began when NO conversion started. N_2O formation seems to be more favored at lower temperatures because its selectivity decreased from 27% to 2% when the reaction temperature was increased from 50 to 250 °C. Above 300 °C, no any N_2O was produced, accordingly, N_2 selectivity increased from 73% to 100%. In such a condition, NO conversion was always higher than CO conversion.

Table 7
Activity and selectivity of NO reduction by CO over the 3%Pd/ZrO_2 catalyst in the oxygen-absent condition

Temperature (°C)	CO conv. (%)	NO conv. (%)	Selectivity (%)		
			N_2	N_2O	NO_2
50	3	11	73	27	0
100	12	23	81	19	0
150	41	56	87	13	0
200	58	67	95	5	0
250	62	70	98	2	0
300	66	75	100	0	0
350	71	79	100	0	0
400	79	82	100	0	0

Factors influencing the reaction mechanism of NO reduction and CO oxidation are complex that usually include the catalyst (support and catalytic active sites) along with reaction condition (temperature, composition of the reaction feed, etc.). The data obtained from the Rietveld refinement shown in Table 5 confirm that many defects exist in the crystalline structure of zirconia support. Around these defects, some oxygen ions are not fully bounded and, they are mobile compared to fully bounded ones. These lattice oxygen ions may be released to form free-like oxygen species by breaking the M–O bond when additional energy is supplied. In oxygen-absent case, when CO adsorbs on the surface of a catalyst where the defective zirconia is the support, these free-like oxygen species may transfer from the bulk to surface, to react with the adsorbed CO and yields CO_2. Therefore, the fast lattice oxygen transport within the defective zirconia is one of the plausible origins of the low light-off behavior for CO oxidation on the Pd/ZrO_2 in the case of oxygen absence from the reaction mixture.

In the reduction of NO, metallic Pd takes a key role. It is reported that NO may preferentially adsorb on the metallic Pd clusters where it is dissociated to yield N* and O* surface intermediates [32–34]. The ability of Pd to dissociate the adsorbed NO, from an electronic point of view, might be resulted from the *d*-electrons from 4d atomic orbital in Pd atoms back-donation to the $2\pi^*$-antibonding orbital of adsorbed NO molecule, that activates the NO–Pd complex and weakens the bond of N–O, and finally it results in N–O bond breaking. It is reported that the energy demanded for NO dissociation is much lower than that for CO dissociation on a variety of metal or metal supported catalysts, the energy for NO dissociation is only 60% of that for CO dissociation in both low ($T < 250$ °C) and high ($T > 250$ °C) reaction temperature ranges [35]. This is in agreement with the fact that conversion of NO is always higher than CO at the same reaction temperature when the reaction mixture does not contain oxygen.

In the case of the inlet mixture without oxygen, N_2O was formed but its selectivity decreased with the reaction temperature increasing. At a temperature above 250 °C, N_2O completely disappeared. This is expected because, at a low reaction temperature, NO dissociation is low and some NO may recombine with surface N* species to form N_2O. It is also possible, on the other hand, that increasing reaction temperature induces the metallic Pd catalyzing the forward reaction of $N_2O + CO \rightleftarrows N_2 + CO_2$, which accelerates the N_2O decomposition and thus decreases N_2O selectivity until disappearance

at high temperature. Accordingly, the N_2 selectivity is enhanced to 100% at a temperature above 300 °C.

It should be pointed out that in the whole reaction temperature range between 50 and 400 °C, NO_2 was not produced at all in the condition of oxygen-absent from the inlet mixture. This can be easily understood that, in a reducing condition, the most favored reaction is the recombination of two adsorbed N* atoms to give N_2 but not the oxidation of NO reaction to produce NO_2.

Because no any oxygen was supplied from outside the reaction system in the case of oxygen absence from the inlet mixture, the oxygen consumed for CO oxidation must come from the zirconia support, i.e., surface lattice oxygen and free-like oxygen ions located the defects in the bulk of zirconia, or/and oxygen from NO dissociation catalysed by metallic Pd. Since the population of the surface lattice oxygen and free like oxygen species in the bulk of zirconia is limit, the oxygen species produced by NO dissociation is mainly responsible for CO oxidation. In this sense, CO conversion is strongly dependent of NO dissociation, which is the key step determining CO oxidation. The catalytic experiments reveal that NO conversion is always higher than that of CO in the case of absent oxygen case. Apart from the effect of competitive association of CO and NO taking place on the Pd surface, another possible reason leading to low CO conversion is that not all the oxygen species generated from NO dissociation move to the sites where CO are adsorbed, to oxidize CO to CO_2. Some of oxygen species might be stored in oxygen vacancies in the bulk of zirconia by forming lattice oxygen.

3.7.2. In the oxygen-rich oxidation

In the oxygen-excess condition (Table 8), the light-off temperature ($T_{50\text{-CO-O}}$) of CO oxidation was between 120 and 150 °C which is lower than $T_{50\text{-CO-r}}$; while, $T_{50\text{-NO-O}}$ for NO reduction was 150 and 200 °C, which is higher than that $T_{50\text{-NO-r}}$. Below 150 °C, the selectivity to N_2 was 100%. However, when the reaction temperature was above 200 °C, NO_2 was produced but its selectivity was no more than 19%. In the whole reaction temperature range between 50 and 400 °C, no any N_2O was detected in the outlet stream, indicating that in an oxidizing condition, N_2O formation is completely inhibited. It is also noted that the catalyst is more active for CO oxidation than for NO reduction in the oxidizing condition because the CO conversion is always higher than NO conversion.

Table 8
Activity and selectivity of NO reduction by CO over the 3%Pd/ZrO_2 catalyst in the oxygen-excess condition

Temperature (°C)	CO conv. (%)	NO conv. (%)	Selectivity (%)		
			N_2	N_2O	NO_2
50	9	5	100	0	0
100	17	7	100	0	0
150	63	41	100	0	0
200	72	57	97	0	3
250	78	62	91	0	9
300	100	67	90	0	11
350	100	71	85	0	15
400	100	73	83	0	19

In the oxygen-excess condition, no any N_2O is formed in the whole temperature range, indicating that the reaction like $2NO + CO = N_2O + CO_2$ does not occur, or rate of following reaction like $N_2O + CO = N_2 + CO_2$ is so rapid that before N_2O desorption, it is totally consumed. At the second place, as discussed above, from the viewpoint of surface reaction of intermediates, not only NO can be dissociated on the Pd metals to produce adsorbed N* and O* intermediates, but also O_2 can be dissociated to form surface O* species. Therefore, O* concentration in the catalyst surface is much higher in comparison with that produced in the oxygen-absent case. NO_2 may be formed by O* species reacting with the adsorbed NO; however, since the selectivity to NO_2 was less than 19%, therefore, this surface reaction is not the main one. N_2 is produced through a recombination of two adsorbed N* atoms or surface reaction like $NO + N^* = N_2 + O^*$, which can be promoted by O* reacting with CO to yield CO_2. Moreover, it is worthy to note that in the oxygen-rich condition, the metallic Pd atoms might be partially oxidized to $Pd^{\delta+}$, that disadvantages the dissociation of the adsorbed NO, and this lowers NO conversion compared with that achieved in the oxygen-absent condition.

4. Conclusions

The zirconia nanophases with structural defects synthesized by a surfactant-templated method show a mesopore texture that progressively varies with calcination temperature. The *in situ* FT-IR and TG analyses confirm that most of the cationic surfactants interacting with the network of the solid could be removed by heating the sample in air at approximately 500 °C. The surfactant linking the solid network may result in crystalline defects formation and structural distortion. The resultant zirconia consists of tetragonal and monoclinic phases having an average crystallite size less than 27 nm at 800 °C. A phase transformation from tetragonal to monoclinic takes place above 600 °C of calcination. When CO adsorbs on the surface of Pd/ZrO_2, various linear CO–Pd^0, CO–$Pd^{\delta+}$ and CO–Zr^{4+} complexes along with CO_2 could be formed. In the oxygen-absent condition, NO conversion over the Pd/ZrO_2 catalyst reaches 82% with selectivity to 100% N_2 above 300 °C. N_2O is formed only in the reducing condition but its selectivity is sensitive to reaction temperature. In the oxidizing condition, the catalytic activity for NO reduction decreases compared with that obtained in the reducing condition. NO_2 is produced with a selectivity less than 18%. CO oxidation is significantly dependent of NO dissociation and reaction condition.

Acknowledgments

This work was sponsored with an international collaboration funding (Grant No. J200.489/2004) granted by CONACyT (Mexico)-NSF (China) and China 973 program (Grant No. 2004CB720603) by China Ministry of Science and Technology. L.F. Chen wishes to acknowledge the scholarship for her

doctorate study sponsored by the CONCyT-Mexico. The authors are greatly thankful to Dr. M. Morán-Pineda and Dr. J. Navarrete for their technical assistances in the FTIR measurement.

References

[1] M. Hino, S. Kobayashi, K. Arata, J. Am. Chem. Soc. 101 (1979) 6439.
[2] M. Misono, T. Okuhara, Chemtech. 23 (1993) 23.
[3] T. Yamaguchi, Appl. Catal. 61 (1990) 1.
[4] X. Song, A. Sayari, Appl. Catal. A: Gen. 110 (1994) 21.
[5] M. Nitta, H. Sakoh, K. Aomura, Appl. Catal. 10 (1984) 215.
[6] E. Devers, C. Geantet, P. Afanasiev, M. Vrinat, M. Aouine, J.L. Zotin, Appl. Catal. A: Gen. 322 (2007) 172.
[7] M.A. Cortés-Jácome, J.A. Toledo, C. Angeles-Chavez, M. Aguilar, J.A. Wang, J. Phys. Chem. B 109 (2005) 22730.
[8] C.T. Young, J.D. Bode, Paper No. 790143, SAE Congress, Detroit, February (1979).
[9] E.C. Subbarao, H.S. Maiti, Adv. Ceram. 24 (1998) 731.
[10] C.B. Alcock, Mater. Sci. Res. 10 (1975) 419.
[11] W. Jeffrey, Fergus Sens. Actuators B: Chem. 121 (2) (2007) 652.
[12] M. Piacentini, M. Maciejewski, A. Baiker, Appl. Catal. B: Environ. 72 (2007) 105.
[13] Y.Y. Huang, T.J. McCarthy, W.M.H. Sachtler, Appl. Catal. 148 (1996) 135.
[14] U. Ciesla, S. Schacht, G.D. Stucky, K.K. Unger, F. Schüth, Angew. Chem. Int. Ed. Engl. 35 (1996) 541.
[15] U. Ciesla, M. Fröba, G.D. Stucky, F. Schüth, Chem. Mater. 11 (1999) 227.
[16] A. Sayari, P. Liu, J.S. Reddy, Mater. Res. Soc. Symp. Proc. 431 (1996) 101.
[17] J.A. Wang, M.A. Valenzuela, J. Salmones, A. Vázquez, A. García-Ruiz, X. Bokhimi, Catal. Today 68 (2001) 21.
[18] X. Song, A. Sayari, Catal. Rev. -Sci. Eng. 38 (1996) 329.
[19] O. Bernard, A.M. Huntz, M. Andrieux, W. Seiler, V. Ji, S. Poissonnet, Appl. Surf. Sci. 253 (2007) 4626.
[20] J.L. Blin, L. Gugot, A. Léonard, B.L. Su, Stud. Surf. Sci. Catal. 141 (2002) 257.
[21] J.A. Wang, J.M. Dominguez, A. Montoya, S. Castillo, M. Moran, X. Bohkimi, Chem. Mater. 14 (2002) 4676.
[22] J.A. Wang, O. Novaro, X. Bokhimi, T. López, R. Gómez, J. Navarrete, M.E. Llanos, E. López-Salinas, J. Mol. Catal. A: Chem. 137 (1999) 239.
[23] Margarita Schneider EDV-Vertrieb, Sarnbergweg 18 D-8134, Pöcking, Germany, 1992, Tel.: +0049 8157 8727; fax: +0049 8157 4527.
[24] R.A. Young, A. Sakthivel, T.S. Moss, C.O. Paiva-Santos, J. Appl. Crystallogr. 28 (1995) 366.
[25] L.J. Bellamy, The Infra-Red Spectra of Complex Molecules, Methuen, London, 1962.
[26] V. Ivanov, E. Zausa, Y. Ben Taârit, N. Essayem, Appl. Catal. A: Gen. 256 (2003) 225.
[27] A. Trovarelli, F. Zamar, J. Llorca, C. De Leitenburg, G. Dolcetti, J.T. Kiss, J. Catal. 169 (1997) 490.
[28] R.M. Davis, B. McDermott, C.C. Koch, Met. Trans. A 19A (1998) 2867.
[29] J. Raskó, J. Catal. 217 (2003) 478.
[30] M. Fernádez-García, A. Martínez-Arias, A. Iglesias-Juez, A.B. Hungría, J.A. Anderson, J.C. Conesa, J. Soria, Appl. Catal. B: Environ. 31 (2001) 39.
[31] D. Tessier, A. Rakai, F. Bozon-Verduraz, J. Chem. Soc. Faraday Trans. 88 (1992) 741.
[32] S.B. Schwartz, L.D. Schmidt, J. Phys. Chem. 92 (1988) 389.
[33] M. Shelet, G.W. Graham, Catal. Rev. -Sci. Eng. 36 (1994) 433.
[34] J.A. Wang, A. Cuan, J. Salmones, N. Nava, S. Castillo, M. Morán-Pinena, F. Rojas, Appl. Surf. Sci. 230 (2004) 94.
[35] E. Giannakas, A.K. Ladavos, P.J. Pomonis, Appl. Catal B: Environ. 49 (2004) 147.